1

Quantitative Phase Microscopy Using Wavefront Analysis

Serge MONNERET[1], Julien SAVATIER[1] and Pierre BON[2]
[1]*Aix-Marseille Université, CNRS, Centrale Marseille, Institut Fresnel, France*
[2]*Université de Limoges, CNRS, XLIM, France*

1.1. Introduction

The observation of transparent samples using optical techniques may seem by definition not very obvious, since these samples have very little influence on the transmission of light that travels therethrough. Consequently, it is necessary to employ more complex solutions than simple imaging in order to reveal the structures of such samples. Interest in such techniques is particularly heightened in biological imaging, for which the observation of living biological cells placed in an aqueous medium leads to very low contrasts, whereas the observation of subcellular structures is of major relevance for the understanding of living organisms. The first techniques developed were based on the use of interferometry to create contrast, but at the cost of relatively complex systems and/or not allowing measurements (contrast increase only). We will present here a technique based on a wavefront measurement, producing a map of the

For a color version of all the figures in this chapter, see www.iste.co.uk/fournier/unconventional.zip.

Unconventional Optical Imaging for Biology,
coordinated by Corinne FOURNIER and Olivier HAEBERLÉ.

optical thickness of the imaged sample resulting in inferring a set of measurements of interest.

1.2. Description of the principles used in phase imaging

We consider an infinite translucent medium (e.g. glass with a refractive index n_0 = 1.5) when a sinusoidal monochromatic light wave of wavelength λ_0 passes through, as shown in Figure 1.1. Consider that this block of glass possesses two internal zones. The first one, in green in the figure, is absorbing and has the same index n_0. The second one, in blue, is transparent but of index $n = n_0 + \Delta n$. If this object is imaged, the green zone that made photons disappear by absorption will create a darker zone than the rest of the image and will consequently be detectable by creating an absorption contrast. On the other hand, the blue zone will not be visible because the photons that traveled through will all reach the detector. Nevertheless, since the index of refraction is different in the blue zone from that of the surrounding medium, these photons will not have taken the same time to reach this detector and will arrive later or earlier than the others according to the sign of Δn.

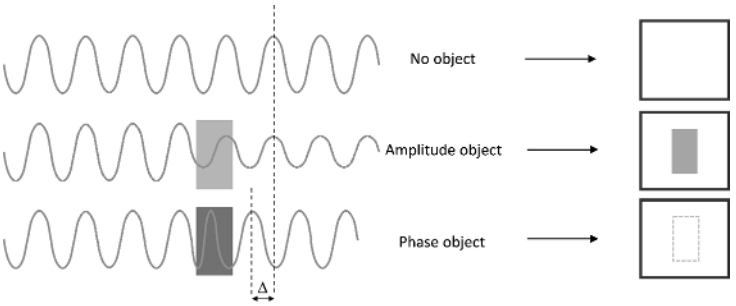

Figure 1.1. *Amplitude and phase in optical imaging*[1]

Let us call Δ the spatial shift of the wave due to passing through the entire blue zone (Figure 1.1). In this simple one-dimensional case, the wave incident on the sample can be written as $A \cos(k_0 x) \exp(-i\omega t)$ where $k_0 = 2\pi/\lambda_0$ is the wavenumber and ω is the angular frequency. The output wave will then take the form:

$$A(x,t) = A\, cos(k_0 x - \Phi)\, exp(-i\omega t)\ with\ \Phi = 2\pi\Delta/\lambda_0 \qquad [1.1]$$

1 Figure developed from: www.microscopyu.com.

The value of Φ is called the phase of the wave, hence imaging techniques that generate contrast from the spatial distribution of the parameter Δ are called phase imaging. It should be noted that the value of Δ can be identical for a low index and large thickness zone, or another zone of higher refractive index but smaller thickness. Consequently, it is the optical thickness (product of the refractive index and the geometrical thickness) which defines Δ, and which will thus be the contrast parameter in phase imaging. Figure 1.2 illustrates the importance, but also the limitations, of phase imaging: it is impossible to decorrelate the optical index from the thickness. Furthermore, a thinner object with a higher refractive index than another can ultimately produce the same phase shift.

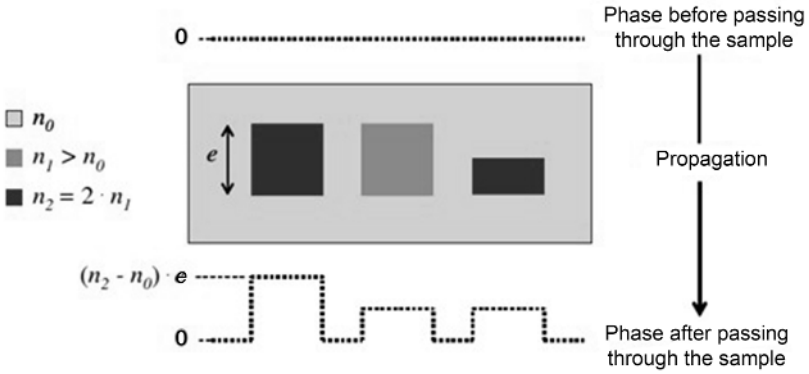

Figure 1.2. *Wave surface deformation when traversing an inhomogeneous object (source: Bon 2011)*

The value of the time shift associated with Δ is tiny (3 fs for every 10 μm crossed for a relative refractive index variation of 0.1) and no current conventional detector can take this time shift into account. Consequently, if they are completely translucent, the red and orange inserts of the sample of Figure 1.2 will be totally undetectable in an imaging system such as a microscope equipped with a conventional camera. On the other hand, making the wave from the sample interfere with another reference wave leads to the creation of an interference contrast that is this time sensitive not to local absorption, but to the parameter Δ and thus to the local optical thickness. Zernike's phase contrast techniques (Zernike 1935), now conventional, as well as Nomarski's contrast techniques (Nomarski 1955), also called *differential interferential contrast* (DIC), are all based on this general principle. Holographic microscopy is probably the most successful version of this principle: it allows access to quantitative information, but requires dedicated microscopes (Cuche et al. 1999).

Consider now a monochromatic plane wave of wavelength λ_0 passing through a phase object considered here as non-diffracting. Its scalar electromagnetic field can be written, after traversal of the object and in a reference plane perpendicular to its mean wave vector:

$$E(x,y) = a(x,y)\ exp(i\ k_0\ W(x,y)) \qquad [1.2]$$

with $a(x,y)$ the amplitude of the field and $W(x,y)$ the distance between the wavefront perturbed by the object and the reference plane wave. Figure 1.3 gives a representation of this surface.

Figure 1.3. *Representation of the W function in a one-dimensional example (source: Bon 2011)*

When illuminating a phased object with an incident plane wave (pictured in Figure 1.2), the wavefront W after traversing the object is directly related to the optical path difference distribution that characterizes this object:

$$W(x,y) = \Delta(x,y) = \int_0^h [n(x,y,z) - n_{med}]\, dz \qquad [1.3]$$

where h is the height of the sample, $n(x,y,z)$ is the refractive index distribution and n_{med} is the refractive index of the surrounding medium.

$W(x,y) = Delta(x,y) = OPD(x,y)$ is called the *optical path difference* in the literature. From now on, we will systematically use this notation in the rest of this chapter.

The knowledge of the distribution $OPD(x,y)$ thus provides us with a complete understanding of the constitution of the object traversed by an incident plane wave. In other words, if we consider that the inhomogeneities within the sample introduce local photon delays with respect to one another, sending a plane wave on this sample will result in producing a distorted wavefront as a result of propagating within these inhomogeneities. The technique we propose here consists of simply measuring the

wavefront after the sample perturbation, using a wavefront sensor, and then deducing the optical thickness mapping of this sample knowing beforehand the shape of the incident wavefront. This technique has been made possible by the emergence of wavefront sensors with sufficient resolution to produce useful information for biologists.

1.3. Quadriwave lateral shearing interferometry for high spatial resolution wavefront analysis

Wavefront analysis using *quadriwave lateral shearing interferometry* (QLSI) is a technique that can be used to meet the objectives presented above.

It is based on the measurement of the gradient of the wavefront simultaneously in two orthogonal directions. To this end, four replicas of the electromagnetic field shifted from each other in the two directions of the analysis plane (Figure 1.4) will be generated by a specific diffraction mask. The interference between these replicas will create an intensity modulation (interference fringes forming what will be called an interferogram, recorded by the sensor of a digital camera) carrying the information of the phase gradients. Post-acquisition analysis of the recorded interferograms then allows for the calculation of the shape of the incident wavefront on the diffractive mask.

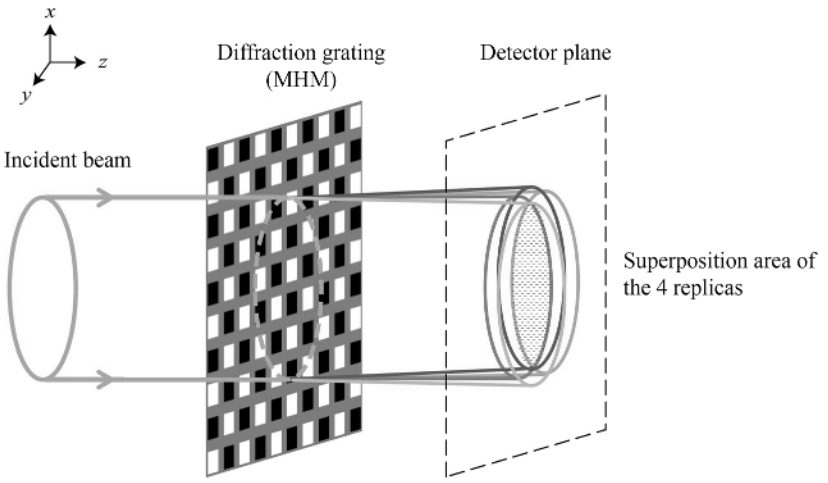

Figure 1.4. *Separation of the incident wavefront into four symmetric replicas along two perpendicular axes by diffraction on a modified Hartmann mask (MHM) (source: Aknoun 2014)*

1.3.1. *Generation of incident field replicas*

As we have just stated, quadriwave lateral shearing interferometry is based on a measurement of wavefront gradients along two perpendicular directions, from the analysis of the interference pattern produced on the sensor of a camera by four replicas of this wavefront slightly inclined along these two directions.

The optical element making possible the generation of these four diffraction orders is a sinusoidal phase grating of transmittance $t(x, y)$ in the two spatial directions. Equation [1.4] describes this transmittance for a grating of period p along x and y; Figure 1.5 presents this theoretical phase grating (Figure 1.5(a)) as well as its diffraction orders (Figure 1.5(c)):

$$t(x,y) = cos(\frac{2\pi}{p}x)\ cos(\frac{2\pi}{p}y) \qquad [1.4]$$

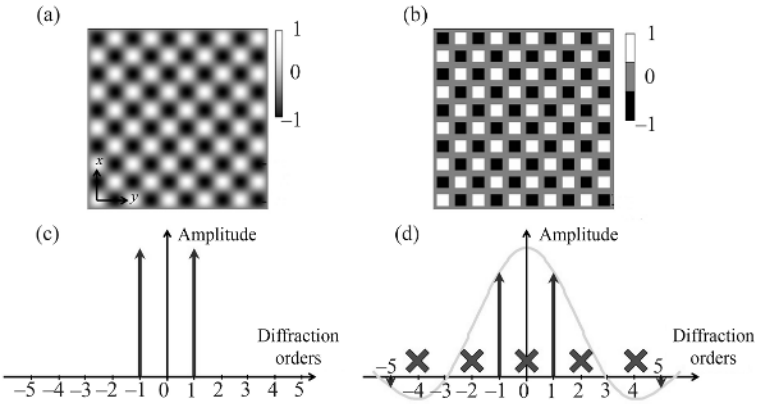

Figure 1.5. *Bisinusoidal phase grating (a) and modified Hartmann grating (b). Graphs (c) and (d) represent the diffracted amplitude distribution in the different orders of these two gratings, respectively (source: Bon 2011)*

Building such a grating is nevertheless difficult. The chosen solution is based on a three-level approximation (+1; 0; 1) of the transmittance function (Figure 1.5(b)). This grating is called a modified Hartmann mask (MHM); it can be seen as the combination of a matrix of square apertures (called the Hartmann mask) and a phase checkerboard dephasing one hole out of two of π. Figure 1.5(d) shows the orders diffracted by an MHM. The choice of a duty cycle of 2/3 results in suppressing orders 3 and –3. The addition of the pure phase grating enables, by destructive interference, the suppression of all even orders, including the zeroth order representing the field not diffracted by the

grating. Therefore, an MHM is a good and practical model of the optimal bisinusoidal phase grating. It enables 90% of the diffracted energy in the four desired orders to be distributed, the rest being distributed in odd orders higher than 3. Nevertheless, its main drawback is that it does not provide as much transparency as the optimal two-dimensional phase grating.

The π phase shift of the checkerboard is obtained by increasing the optical path traveled, that is, the grating is locally thicker to introduce the desired delay. Relation [1.5] links the difference in thickness e to the optical index n of the material used to create this π phase shift:

$$e = \frac{\lambda_0}{2(n-1)} \qquad [1.5]$$

This relation shows the obvious dependence of the etching thickness on the usage wavelength of the grating. When the phase shift is not exactly π, a reoccurrence of the even orders is observed, and in particular of zeroth order. These orders will interfere with the useful orders and will create additional frequencies in the interferogram, degrading the signal-to-noise ratio. It is however possible to find distances between the mask and the plane of the detector, minimizing the influence of the parasitic orders (Primot and Guérineau 2000): in these planes, the interferogram is similar to that which would be obtained for a phase shift of π. In practice, when light is not monochromatic, e should be chosen so as to create a phase shift of pi for the central wavelength of the source and a mask/detector distance close to the Talbot distance of the Hartmann mask for this central wavelength (Velghe 2006).

This operating point makes it possible to obtain an achromatic assembly operating regardless of the wavelength spectrum of the source, including white light. This is a major advantage of the technique applied to microscopy, since it enables us to use the conventional illumination of the microscope to perform the measurement (halogen source sufficiently spatially coherent to generate the interferograms, used in a Köhler assembly with a reduced aperture diaphragm).

1.3.2. *Determination of the incident wavefront*

As we have seen above, after a few millimeters of propagation, the beams are slightly separated and then form interference fringes whose pitch is determined by the angle between the propagation directions. If the incident beam is a perfectly plane wave, the interferogram recorded by a camera is a regular two-dimensional array of light points. If the wavefront presents local modulations, this regular mesh is locally deformed. The study of these distortions using spectral analysis methods allows us to find the phase spatial gradients.

More precisely, the intensity distribution at the level of the interferogram, after propagation along a distance z after passing through the mask (placed in the plane z = 0), is given by (Bon 2009):

$$I(x,y,z) = I_0 \left[1 + cos\left(\frac{2\pi}{p}x + \frac{2\pi}{p}z\frac{\partial OPD}{\partial x}\right) + cos\left(\frac{2\pi}{p}y + \frac{2\pi}{p}z\frac{\partial OPD}{\partial y}\right)\right] + \frac{I_0}{2}\left[cos\left(\frac{2\pi}{p}(x+y) + \frac{2\pi}{p}z\frac{\partial OPD}{\partial (x+y)}\right)\right] + \frac{I_0}{2}\left[cos\left(\frac{2\pi}{p}(x-y) + \frac{2\pi}{p}z\frac{\partial OPD}{\partial (x-y)}\right)\right] \quad [1.6]$$

where I_0 corresponds to the maximum intensity on the diffraction mask output. This equation corresponds to a perfect mask generating only the four desired diffraction orders.

This equation shows that various wavefront gradients are encoded in the form of frequency modulation around characteristic interferogram spatial frequencies, that is, the eigen spatial frequencies of the MHM.

Let us now consider an arbitrary wave arriving at the MHM at normal average incidence. If we merely consider a single dimension to simplify the equations, the intensity recorded at the detector can be written as:

$$I(x) \approx i_0(x) + i_x(x)\, cos\left(\frac{2\pi}{p}\left[x - L\,\frac{\partial W(x)}{\partial x}\right]\right) \quad [1.7]$$

where L is the distance between the MHM and the camera sensor. This coefficient, placed in front of the wavefront gradient term, is important: it can be used to modulate the sensitivity to gradients (the larger L is, the more sensitive the sensor, however it provides less dynamics).

The gradient along the x-direction of the wavefront can be extracted by demodulation in the Fourier space of the interferogram. We call $|\nu_{int}|$ the maximum spatial frequency of the intensity information i_0. We call $|\nu_{mod}|$ the support in Fourier space of the information modulated around the carrier frequency and 1/p the fundamental frequency of the interferogram. T_{pix} refers to the sampling period of the matrix detector (it is assumed that the pixels are square), θ refers to the orientation of the interferogram with respect to the sensor pixel matrix and $\Delta\nu = 2/\alpha p$ refers to the bandwidth for the extraction of the phase information, α being a parameter used to simplify the computations. All of these notations are represented in Figure 1.6.

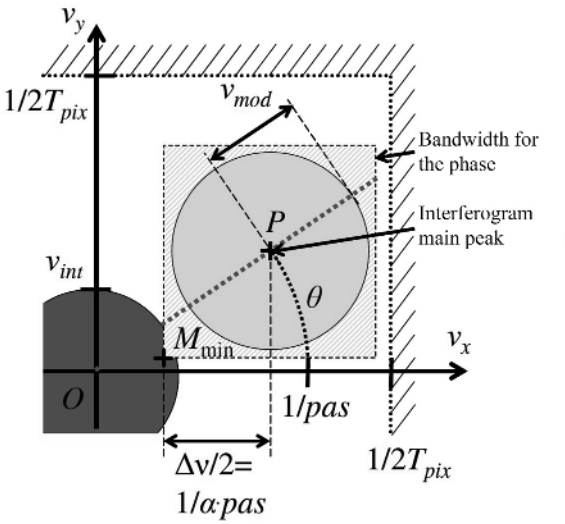

Figure 1.6. *Definition of the various supports in Fourier space (source: Bon 2011)*

Various conditions must be met to ensure that the bandwidth is sufficient, without spectrum aliasing, to accurately reconstruct the phase and intensity signal. First, the main frequency of the grating $cos(\theta)/p$ must be lower than the Nyquist frequency $1/2T_{pix}$ in order to sample the signal correctly; it is also necessary that all the frequencies of the bandwidth around the main frequency satisfy this same Nyquist criterion. Finally, the last condition comes from the necessary non-overlap between the intensity information and the modulated phase information; this must be reflected by a non-overlapping of the red and orange domains of Figure 1.6. It should be noted that for essentially transparent samples, such as those usually employed in the field of cell biology, the energy values (especially for high spatial frequencies) will be lower in intensity than in phase.

In the end, a choice of α = 2 is often made at the level of the reconstruction algorithms to best separate the bandwidth of the frequency support from the intensity distribution of the samples. This choice requires that the phase and intensity images resulting from the reconstruction processes have a number of pixels 16 times lower than the images initially produced on the sensor plane. More precisely, with such a value of α a sensor area of 4 x 4 pixels is used to produce a local phase measurement. The lower limit that would just satisfy the Nyquist criterion would be to use 2.73 x 2.73 pixels to sample the interferogram. Some recent commercial systems utilize a reconstruction algorithm based on 3 x 3 pixel sampling (SID4 SC8, Phasics, France). Finally, equation [1.6] shows that we also have access, through the

interferogram, to the gradients in the (x + y) and (x – y) directions. This redundant information can be used to increase the signal-to-noise ratio of the wavefront measurement (Velghe et al. 2005).

The most commonly used method to quantitatively reconstruct the wavefront employs the discrete Fourier transform, which leads to artifacts when the phase objects overlap the edges of the image, which is common in cell biology. To address this shortcoming, a simple approach has been proposed to avoid these artifacts, based on the duplication and antisymmetrization of the derivative data, in the direction of the derivative, before integration (Volkov et al. 2002; Bon et al. 2012a). This approach completely erases edge effects by creating continuity and a mathematical differentiability condition at the edge of the image.

It is thus possible to extract the OPD gradients from the Fourier analysis of an interferogram recorded on a CCD or CMOS sensor. The gradients are finally integrated to obtain a two-dimensional OPD map. However, since the phase information is encoded in the interferogram by a frequency modulation, the phase and intensity are independently determined. The intensity image is effectively simply extracted from the application of a low-pass filter on the interferogram (fringe descreen operation). This property offers an advantage over conventional phase contrast methods such as Nomarski/DIC or Zernike contrast, where it is very difficult to attribute the intensity modulations visible in the images either to a spatial variation of the sample absorption or to OPD gradients.

1.3.3. *Wavefront sensor implementation*

The technology of wavefront measurement using quadriwave lateral shearing interferometry until now has been exclusively commercialized by Phasics (Saint-Aubin, France), a company that holds the exploitation rights. The various products developed over the last 20 years have followed some of the technological evolutions of cameras (including the shift from CCD cameras to sCMOS cameras, the development of sensors for specific spectral domains such as infrared), making it possible to address ever wider application fields. Nonetheless, some applications still require very specific cameras (EMCCD in very low light, ultrafast cameras for the measurement of dynamic samples, etc.) to acquire interferograms. The now commercialized (SID4Element, Phasics, France) proposed solution (Berto et al. 2012) consists of using an imaging optical system as a relay to project the image of an MHM, at the appropriate location and magnification, inside the camera optimized for the targeted application. Consequently, it is possible to acquire interferograms under very low light to achieve phase images in full-field coherent Raman microscopy, or to use a fast camera to follow fast-evolving samples (see section 1.5.3).

1.4. Using a wavefront sensor in microscopy

Most non-tissue biological objects (isolated biological cells in culture) appear very faintly in intensity-based imaging (otherwise known as absorption imaging). In this case, when the incident light exits the sample it has undergone a phase shift only (hence the name phase objects sometimes used), and therefore its wavefront has been modified. Placing a wavefront sensor on the sample output should thus allow the optical thickness of the sample to be mapped, and thus a contrast of interest to be generated.

1.4.1. *Necessary approximations*

We consider a simple model for interpreting the measured difference values of the optical path, overlooking the imaging and filtering effects by the microscope objective. The first approach that we can follow for interpreting the measurements consists of considering that at first order, the measured phase shift is due only to photons slowing down when passing through the sample and that no change in direction of propagation occurs during the traversing. Any refraction phenomenon at the interfaces or diffraction by the object is not taken into account: refraction is negligible with small index differences or if the interfaces are orthogonal to the propagation of light; diffraction is visible when the objects become small relative to the resolution limit of the microscope. Under these assumptions, the wavefront sensor directly measures the optical path difference within the sample, according to the diagram in Figure 1.3.

This assumption considers that all photons propagate in the same direction, which is that of the optical axis of the system; the illumination is said to be plane wave illumination. In fact, all of the measurements will be performed following a quasi-planar wave illumination regime via a diameter restriction of the aperture diaphragm of the Köhler illumination of the microscope.

It seems that the simple measurement of the wavefront shape on the sample output provides us with a map of the optical thickness of the sample. In real life, and in particular inside a microscope, it is unrealistic to generate a perfectly plane wavefront incident on the sample. Consequently, we must also record the shape of this incident wavefront – a step that will be called “reference analysis” – which is performed at the beginning of the experiment. It is a priori not necessary to repeat this step as long as the experimental conditions are not modified (temperature, microscope settings, non-uniform conditions at the sample level). The modifications of the wavefront due to the sample, relative to this reference wavefront, will then give the local optical thickness map being sought.

1.4.2. *Experimental configuration*

Figure 1.7 shows the conventional experimental configuration for quantitative phase imaging by wavefront measurement using a wavefront sensor from QLSI technology. This sensor, consisting of the MHM and a CCD camera, is placed on the video output port of a microscope. In fact, all of the images obtained in the following sections will have been obtained from different commercial sensors, whose type will be specified for each case. The CCD sensor of the wavefront sensor is placed in the focal plane of the microscope tube lens so that the sample is imaged on the detector. In fact, the sensor essentially consists of a camera inside which the MHM is inserted. Consequently, its use is identical to that of a conventional camera in terms of handling and fixing on the microscope (C mount). The measurement of the incident light wavefront on the sensor (illumination beam, in green + components due to diffraction by the object, in red) is then carried out according to the methodology explained previously. It is also represented in Figure 1.8, which specifically illustrates the process of quantitative imaging of biological samples.

This figure, taken from Aknoun (2014), effectively resumes the main steps of the reconstruction process of an optical thickness map for a biological sample (here, a living COS-7-type biological cell, the lineage resulting from a kidney of a green monkey from Africa). A recording of the interferogram, which can be seen in the figure, shows the disturbing effect of the presence of inhomogeneities in the sample on the regular alignment of the interference fringes. Then, a spectral demodulation of this interferogram in Fourier space makes it possible to recover the intensity image and to obtain the phase gradients due to the sample in two perpendicular directions. Integration from these two gradients finally results in reconstructing a quantitative phase map of the object. Since the local modulation of the interferogram interfringe is only caused by the local phase shift of the wavefront, and not by its intensity, the phase and intensity measurements are completely uncorrelated. During the whole process, the commercial algorithms used (SID4Bio software, Phasics, France) take into account in an optimal way the preliminary recording of a reference interferogram, acquired from an empty part of the sample under the same conditions used for the latter. As such, only the OPD map due to the sample can be displayed, independently of the characteristics of the light beam that may vary according to the conditions under which the optical system is used. It should be noted that the native light source of the microscope (white halogen lamp, or white LED depending on the microscope used) is employed to make the images due to the achromatic character of the technique. However, it is sometimes useful to use spectral bandpass filters or LEDs of different colors to perform certain measurements in better defined spectral domains, when the application requires it (sensitivity to sample chromaticity, typically).

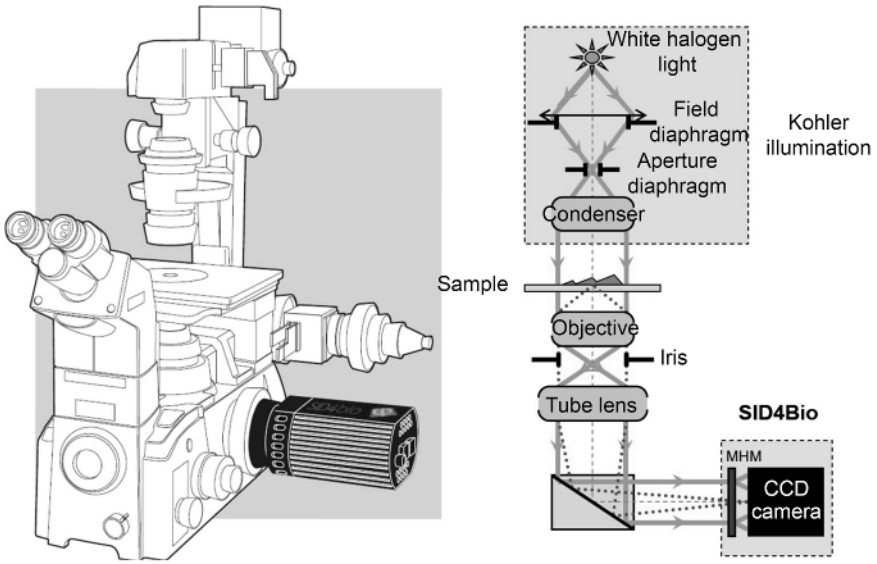

Figure 1.7. *Conventional optical configuration for quantitative phase imaging by QLSI*

1.5. Applications to biological imaging

1.5.1. *High-contrast imaging without labeling*

The first contribution of this imaging technique is to offer remarkable phase contrast, without halo (characteristic of Zernike phase contrast when used without apodized mask) or unidirectional gradient (characteristic of the Normarski/DIC process). Biological samples show sufficient local refractive index inhomogeneities to reveal their internal structure, even when the traversed thicknesses are small. The sensitivity in OPD, of the order of 0.1 nm, is sufficient to clearly characterize the plasma membrane, mitochondria, different types of vesicles (lysosomes, peroxisomes, endosomes, at least a good part of each of them) and of course the nucleus and chromosomes during cell division. It is also possible to distinguish components of the cytoskeleton, such as microtubules and some actin stress fibers, at least in fairly thin areas of the cell further away from the nucleus (Bon et al. 2014). This contrast quality, without even enhancing the quantification inherent to the technique, is already very useful in cell biology to appreciate the state of the cells under the microscope and the results of different treatments (drugs, temperature, illumination at different powers and wavelengths) (Figure 1.9). Similarly, by following the cellular and intracellular dynamics over time, at frequencies that can reach several Hz, the cellular metabolism can be evaluated.

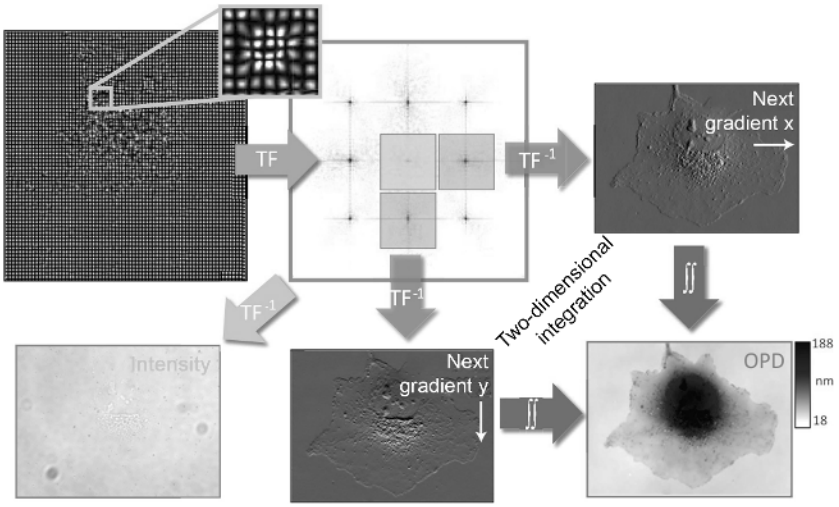

Figure 1.8. *Main steps for reconstructing an OPD distribution from an interferogram recorded by a wavefront sensor (source: Aknoun 2014)*

1.5.2. *Dry mass measurement in living biological cells*

In some specific cases, an optical path difference measurement can provide information about the amount of material present in the sample. For amorphous or crystalline solids, a linear increase in the density of the material is reflected by a linear increase in the real part of the refractive index. Similarly, in the case of a solution, increasing the mass concentration of a solute in a solvent produces a proportional increase in the solution refractive index, according to a coefficient that depends on the solute. Nevertheless, even for biological cells containing a large number of constituents (proteins, lipids, sugars, nucleic acids, etc.), it has been demonstrated that for most eukaryotic cells, considering a single and generic coefficient relating the solution refractive index to the solute mass was valid (Barer 1952).

Consequently, the cell dry mass m, defined as the sum of the masses of any non-aqueous constituent, can be directly calculated from the integral of the distribution of the cell OPD over its projected surface:

$$m = \frac{1}{0.18} \int_S OPD(x, y)\, dxdy \qquad [1.8]$$

where mass is given in picograms, and the integral corresponding to a volume is calculated in μm^3. The coefficient of 0.18 μm^3.pg^{-1} is the most commonly used in

general by the scientific community dealing with quantitative phase measurement and it can only vary for some particular cell lines. For example, it is equal to 0.19 $\mu m^3.pg^{-1}$ for red blood cells considering that this cell type contains a high hemoglobin content.

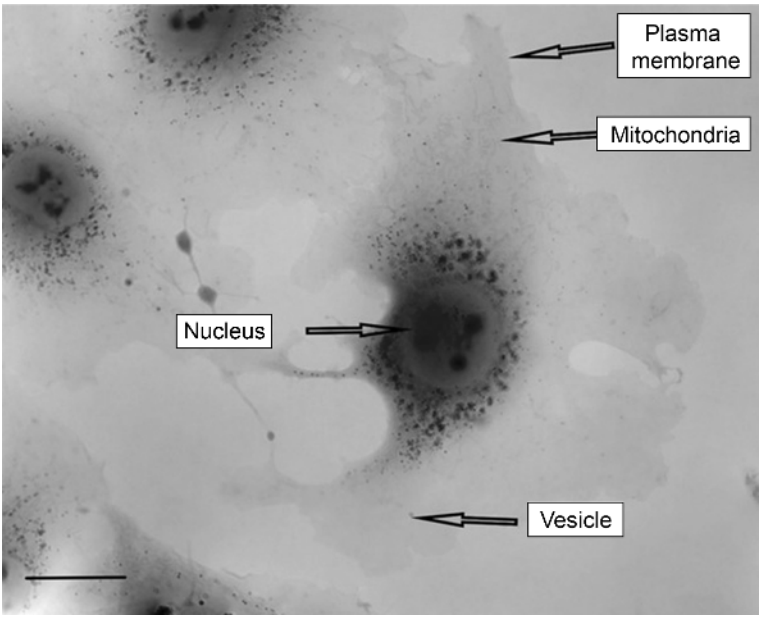

Figure 1.9. *COS-7 cells in culture at $37°$C. Quantitative phase image taken with the SID4 HD prototype (2560 x 2160 phase pixels), 100X, NA = 1.3. Scale bar: 10 μm*

The integration of the OPD on the cell surface requires automatic segmentation of the cell edge to define this surface. This operation is facilitated by the fact that the images are of good quality and especially free of halo around the cells. Even in the thinnest areas of the cell edge, where the OPD corresponds only to the plasma membrane composed of a phospolipid bilayer folded over itself, the contrast generated is sufficient for the segmentation algorithm to correctly identify the cell edges. This algorithm, developed jointly with Frédéric Galland (Institut Fresnel, Phyti team), not only allows for this edge detection but also a calibration of the OPD levels. As a matter of fact, it includes a so-called background flattening phase, that is, the possibly local measurement of the residual OPD level between the cells (defined as the image "background"), which will then be used to calibrate the dry mass. The reference analysis step is in fact not efficient enough to ensure zero residual given the sensitivity

of the technique. The developed algorithm thus allows the computation of dry mass values that are very accurate and close to biological reality (Aknoun et al. 2015).

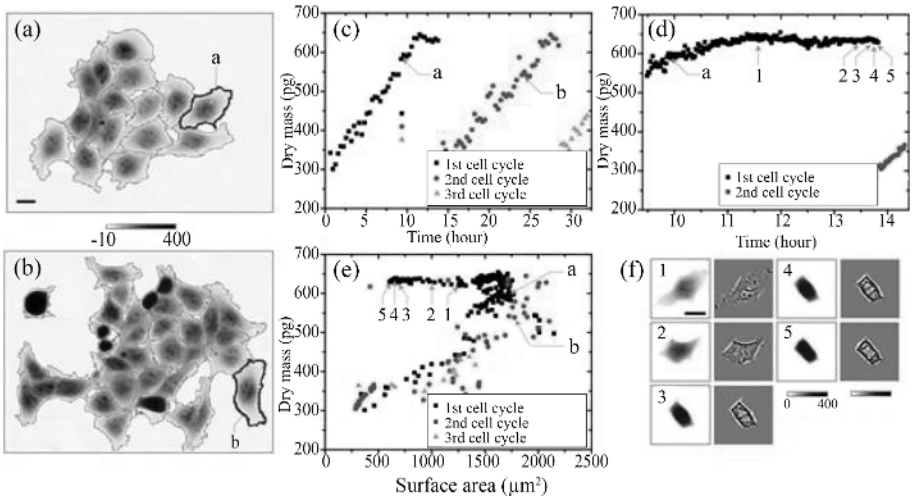

Figure 1.10. *Thirty-four-hour cell cycle monitoring of COS-7 cells*

COMMENTS ON FIGURE 1.10.– *(a) Quantitative phase image taken with SID4Bio, 40X NA 0.75, 37°C and 5% CO_2, scale bar: 20 m. Automatically segmented cells and cell designated by a monitored. (b) Same field of view 15 h later, daughter cell b monitored. (c) Dry mass time monitoring, 1 point every 30 s. Cell a in black, daughter cell b in red. (d) Magnification of the plateau of cell a represented in (c). (e) Representation of the same points in a "projected area versus dry mass" space. (f) Images (raw on the left-hand side and filtered with a high-pass frequency filter on the right side) of cell a at five time points, denoted from 1 to 5 in insets (d) and (e).*

The ability to measure dry mass in an individual living cell by a simple image capture is fundamental, given that it allows the long-term monitoring of dry mass evolution in a cell and/or cell population (Figure 1.10). For example, we have monitored the cell cycle, during which the dry mass of a cell progressively increases until it doubles at the time of mitosis, where it divides into two almost equal daughter cells. Recording a quasi-linear increase in dry mass, before reaching a plateau, is relevant data (Figure 1.10(c)). Each point in this figure is associated with an OPD image of the scene, making it possible to identify which phase of the cell cycle the monitored cell is actually in. This identification is particularly easy at the time of mitosis, where the behavior of chromosomes is visible even at a relatively low magnification of 40X (Figure 1.10(f)).

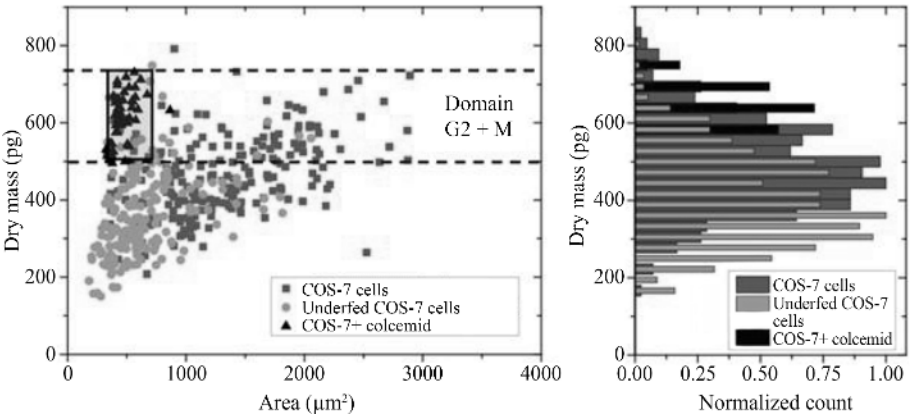

Figure 1.11. *Dry mass and projected area of COS-7 populations. Control cells in red, serum-starved cells in orange and prometaphase-blocked cells in black*

The accuracy of the dry mass measurement, with a standard deviation of the order of 0.2% (Aknoun et al. 2015), enables the impact of treatments on the cells to be highlighted. For example, it is possible to deprive them of feed to a certain extent (percentage reduction of fetal calf serum or FBS in the culture medium, from 10 to 0.5% over 48 h). The metabolic impact of such an action on a cell population is then observed in comparison to control cells (Figure 1.11). The treated cells become smaller, with lower dry mass. Another experiment consists of blocking microtubule polymerization, essential at the time of the separation of the chromosomes between the two future daughter cells (by addition of colcemid, 24 h at 1 mg/L). It is observed that all the cells enter a state of minimal projected surface (they are then spherical) but exhibit maximum dry mass. They are logically blocked in prometaphase. Therefore, from the knowledge of the area/mass characteristics of a given cell population (Figure 1.11(a)), we can statistically classify a cell population according to the cell cycle phases, without the use of labeling. This opens up the possibility of keeping a potential for labeling, for example of the fluorescence type, for the study of other simultaneous cellular functions.

1.5.3. *Rapid imaging for biological phenomena*

We use different QLSI imaging modalities depending on what we want to observe and measure. The primary difference is the sensor. We have the ability to use a high-speed camera, the Phantom Miro M120, which is capable of taking full-field

images at 730 Hz. With a 3 x 3 pixel analysis, quantitative phase images are obtained at 640 x 400 pixels at very high frequency.

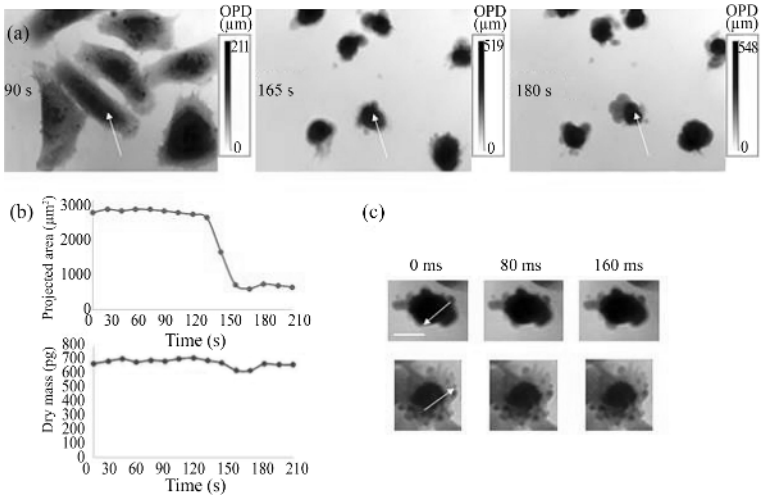

Figure 1.12. *Blebbing in U2-0S cells (human osteosarcoma). Image taken with the fast SID4 element, 40X NA 0.75: (a) one image every 15 s; (b) monitoring of cell projected area and dry mass indicated by white arrow in (a); (c) two cells with blebbing, taken at 100 Hz. Scale bar: 10 μm*

Such a speed allows the observation of very fast phenomena, such as blebbing. This phenomenon corresponds to the prominence of the cell plasma membrane caused by the delocalized uncoupling of the cytoskeleton from the membrane. This sudden onset of blebs, or bulges, is fast and important during division, locomotion or cell apoptosis (programmed cell death). It is not accompanied by loss or gain of material, but by reorganization and flow. It is associated with certain cell types but can be induced by adding calyculin A (20 nM here). If we observe images of cells every 15 s, cells can be seen changing drastically in shape and size, without us understanding what is going on (Figure 1.12(a)). The projected area undergoes an abrupt decrease when the blebbing starts at 120 s of acquisition (Figure 1.12(b)). On the other hand, dry mass remains fairly constant. The cell then changes shape so rapidly that we have no idea where the phenomenon starts each time. If images are taken at higher frequencies, all of the steps can be seen much better and it might be easier to understand the phenomenon more deeply (Figure 1.12(c)). Without reaching up to 730 Hz, a frequency of 100 Hz can also help to average the recordings of interferograms in order to increase the signal/noise ratio, while keeping a high acquisition frequency (100 Hz with seven images, for example).

1.5.4. *Quantitative phase and fluorescence correlative imaging*

Here, we make use of the fact that this technique is achromatic and perfectly usable in the near infrared (NIR) to combine it simultaneously with fluorescence imaging, here in full-field, the latter using the visible spectrum. Figure 1.13 represents the optical scheme of this bimodal imaging. The fact that phase imaging is carried out using transmission while fluorescence uses epi-detection, simplifies the actual simultaneous implementation of the two channels and consequently makes it possible to perfectly superimpose the images acquired by the two cameras (CCD, EMCCD or sCMOS). It is theoretically possible to use a color camera associated with a multiband fluorescence set to simultaneously perform phase imaging and several colors in fluorescence.

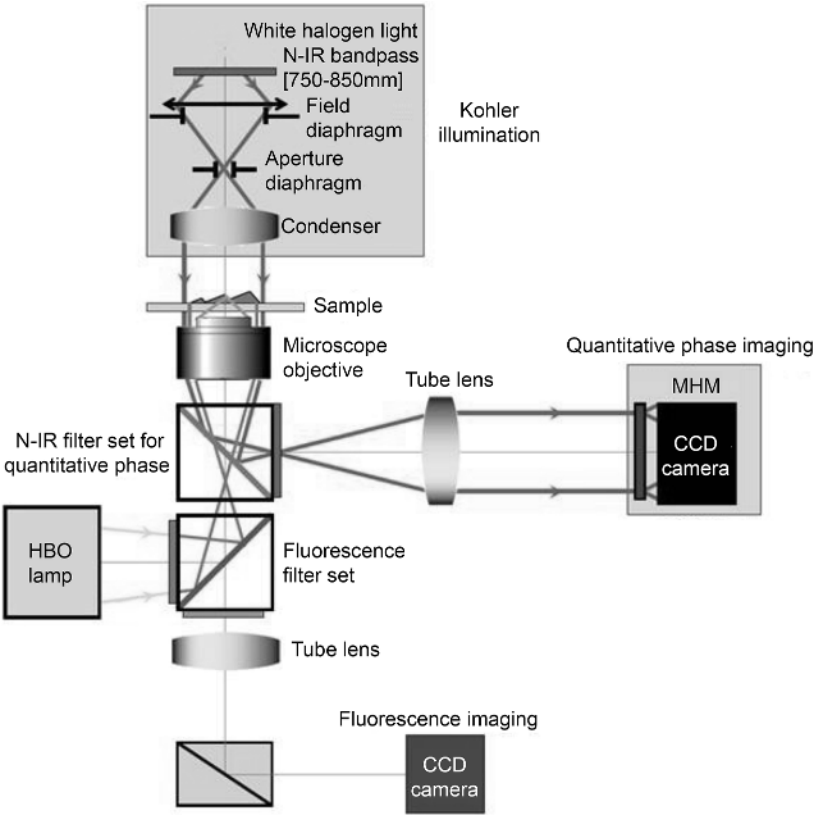

Figure 1.13. *Quantitative phase imaging coupled with fluorescence imaging on a two-stage microscope. The rear video port at the upper stage is used for phase imaging while fluorescence excitation is performed by the lower arm*

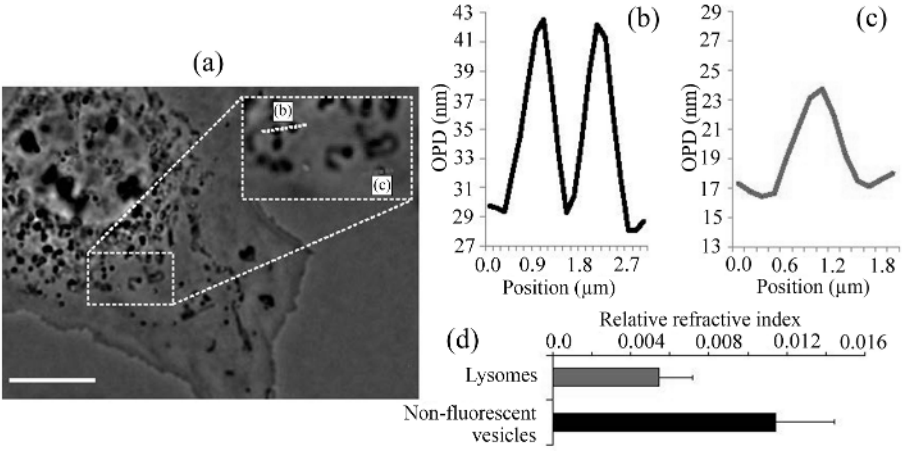

Figure 1.14. *Lysosome quantitative phase imaging compared to other vesicles, in COS-7 cells*

COMMENTS ON FIGURE 1.14.– *(a) An example of phase/fluorescence composite images (in red: RFP, lysosomes), with a magnified view. (b and c) Optical path difference (OPD) profile of vesicles along the white and red dotted lines drawn in (a), respectively. (d) Relative refractive index distribution (Δn/diameter) of fluorescent lysosomes and other non-fluorescent vesicles (mean values and standard deviation), obtained from 70 measurements on independent vesicles of about 1 μm in diameter, showing a significant difference between the two populations. Scale bar: 5 μm.*

We have applied this association to the monitoring and identification of cellular organelles. Fluorescent labeling allowing for optimal specificity and quantitative phase imaging with which a huge number of cellular components can be seen at once; these modalities are perfectly complementary. Figure 1.14(a) illustrates the overlay of a red fluorescent labeling specific to lysosomes as well as quantitative grayscale phase imaging of the overall cell. However, the lysosome labeling does not label all vesicles. A "relative refractive index" of each vesicle considered spherical can then be defined as its OPD divided by its diameter (Figures 1.14(b) and (c)). By computing this relative index from 70 objects of equivalent size (about 1–2 μm, to ensure that we stay above the diffraction limit), a significant difference can be observed between the lysosome population and that of the other vesicles (Figure 1.14(d)).

We also labeled the nucleus and the Golgi apparatus, as shown in Figure 1.15. Again, only one color can be simultaneously taken with the phase, the mitochondria in this case. To better distinguish the overlay, the phase imaging has been inverted to grayscale (the densest optically is the brighter, unlike in Figure 1.14). Mitochondria are still easily detectable in phase imaging.

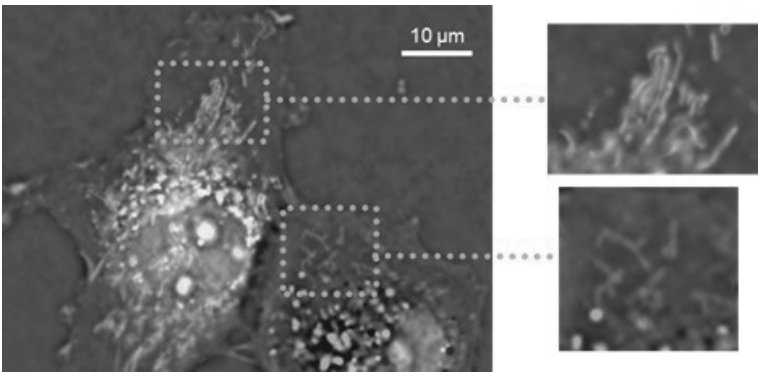

Figure 1.15. *COS-7 labeled at the mitochondria (green), Golgi apparatus (orange) and DNA level, and hence the nucleus (blue), on a grayscale phase imaging background. The cell on the bottom right was not labeled at the mitochondria or Golgi apparatus level due to a transfection rate inducing fluorescent labeling that is not 100%*

1.6. Optical retardance imaging

Until now, to obtain a map of the OPD for a given sample, we have usually measured two successive wavefronts in unpolarized light, namely a first one outside the sample (reference shot) and a second one with sample. The difference between these two measurements gave a map of the OPD of the imaged object (Figure 1.16(a)). A possible variation of the technique consists of using a linearly polarized incident light beam (Figure 1.16(b)). In this case, the first interferogram recording is carried out with polarization along a defined axis, then the second with crossed polarization, perpendicular to the first one. Consequently, if the observed sample is optically isotropic, it will produce the same wavefronts on the sensor. On the other hand, if some area in the sample (blue area on the figure) is optically birefringent, then the refractive index, and thus the retardance, seen by the light field, will be different for the two polarization states under consideration. A comparison between these two wavefronts then allows us to specifically identify any birefringent structure (within the observation plane) of the sample.

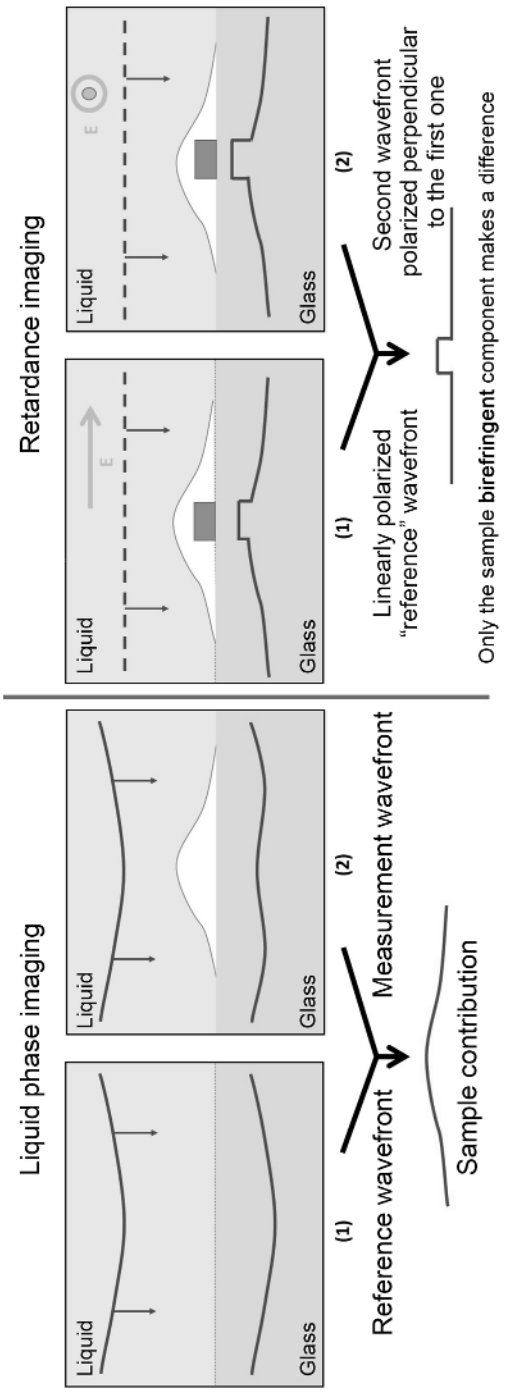

Figure 1.16. *The main reconstruction steps of an OPD distribution from an interferogram recorded by a wavefront sensor (source: Aknoun 2014)*

The evolution of the difference between these two wavefronts depends on the orientations chosen for the crossed polarization axes. Moreover, the orientation of the optical axes of the sample birefringent zones is generally not known. Consequently, it is necessary to perform a set of OPD measurements by varying the linear polarization angle of the beam. As a matter of fact, the OPD of a birefringent medium varies as a function of the angle θ of the polarization direction according to the following equation:

$$OPD(x, y, \theta) = \int_0^h [n(x, y, z, \theta) - n_{med}]\, dz \qquad [1.9]$$

This equation can be rewritten, omitting the spatial coordinates for better readability:

$$OPD(\theta) = \int_0^h (\frac{n_o + n_e}{2} - n_{med})\, dz + \left[\int_0^h (\frac{n_o - n_e}{2})\, dz\right] cos[2(\theta - \theta_0)] \qquad [1.10]$$

where n_o and n_e are the ordinary and extraordinary indexes of the birefringent medium, and θ_0 represents the direction of the principal optical axis of this medium. The first term of the sum giving the OPD corresponds to what would be obtained under unpolarized light, and the second corresponds to a variable part depending on the illumination angle θ.

Figure 1.17(c) shows a typical schematic representation of a curve from six measurements achieved according to six different polarization directions. While the acquisitions can be quickly carried out using automated polarization control systems, the analyses for extracting the retardance maps are much more complex; this is mainly due to the fact that the six OPD images computed for six different polarization angles must be searched for the sine curve crossing the measurement points for each pixel (Figure 1.17(c)). The delay value, for each pixel, is thus obtained as well as the angle θ_0.

Knowledge of these retardance and orientation values can then be used to derive information about the organization of the sample. For example, knowledge of the distribution of θ_0 within amyloid fibers can be used to visualize the organization of these fibers, just as a distribution of retardance in a biological tissue makes it possible to appreciate the orientation of collagen fibers (Figure 1.18), as the signature of the presence of tumor in the tissue (Aknoun et al. 2018).

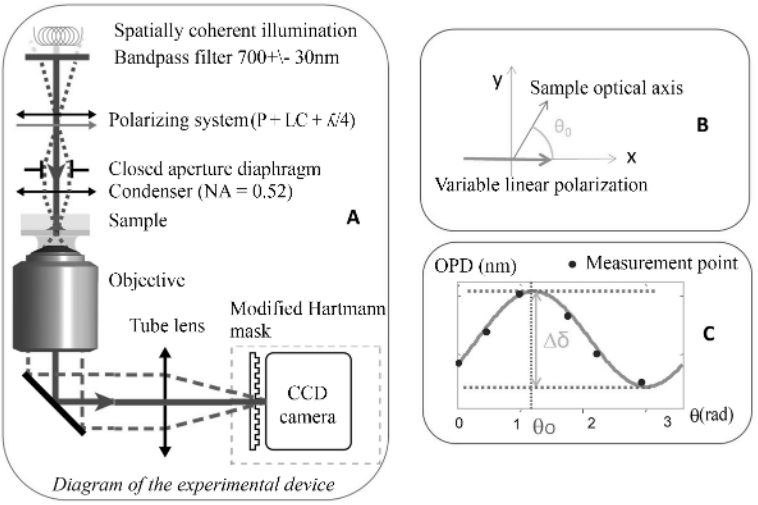

Figure 1.17. *(a) Dedicated retardance imaging configuration. The polarization system is based on liquid crystals enabling control of the polarization direction without mechanical motorization. Representations of the rotating polarization (b) and a typical curve from the measurement points (c)*

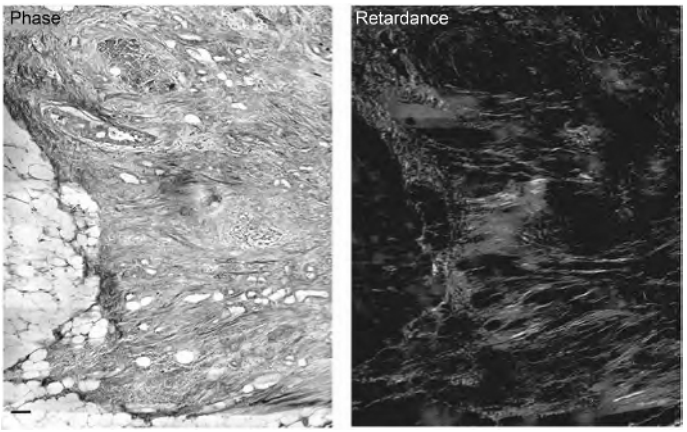

(a) (b)

Figure 1.18. *Example of images obtained from fixed biological tissue. (a) OPD distribution. (b) Optical retardation image showing the presence of collagen fibers whose orientation can be assessed*

1.7. Other applications and new developments

In this chapter, we have focused on the biological applications of the QLSI phase imaging technique. It is nevertheless obvious that this technique can be used with a variety of samples. We can thus clearly identify waveguides buried in a transparent substrate, measure the optical thickness of the core of single-mode optical fiber, that of dielectric thin film up to a graphene monolayer (Khadir et al. 2017). The contactless optical profilometer function is also available, and it has been shown that the technique proves to be particularly effective in detecting very early laser damage (Douti et al. 2015).

Moreover, most liquids, including water, have the property that their refractive index varies with temperature. As such, a hot spot on a sample immersed in water will generate a local perturbation of the water refractive index in the vicinity of the heat source, which can be considered a phase object measurable using the phase imaging technique presented in this chapter. Knowing this phase object, the local temperature can be deduced (Baffou et al. 2012). Therefore, we have been able to demonstrate the possibility of performing local temperature measurements in a sample under a microscope, including control of cell stimulation by temperature (Robert et al. 2018).

Finally, the achromatic character of the QLSI technique is of great interest for measurements under femtosecond illumination, as light pulses of this duration become spectrally broad. We have used this property to visualize the propagation of the Kerr effect within a silica sample in a time-resolved manner (Gallais et al. 2016).

1.8. References

Aknoun, S. (2014). Analyse quantitative d'images de phase obtenues par interféromètrie à décalage quadri-latéral. Applications en biologie. PhD thesis, Aix-Marseille Université, Marseille.

Aknoun, S., Bon, P., Savatier, J., Wattellier, B., Monneret, S. (2015a). Quantitative retardance imaging of biological samples using quadri-wave lateral shearing interferometry. *Optics Express*, 23(12), 16383–16406.

Aknoun, S., Savatier, J., Bon, P., Galland, F., Abdeladim, L., Wattellier, B., Monneret, S. (2015b). Living cells dry mass measurements using quantitative phase imaging with quadri-wave lateral shearing interferometry. An accuracy and sensitivity discussion. *Journal of Biomedical Optics*, 20(12), 126009.

Aknoun, S., Aurrand-Lions, M., Wattellier, B., Monneret, S. (2018). Quantitative retardance imaging by means of quadri-wave lateral shearing interferometry for label-free fiber imaging in tissues. *Optics Communications*, 422, 17–27.

Baffou, G., Bon, P., Savatier, J., Polleux, J., Zhu, M., Merlin, M., Rigneault, R., Monneret, S. (2012). Thermal imaging of nanostructures by quantitative optical phase analysis. *ACS Nano*, 6(3), 2452–2458.

Barer, R. (1952). Interference microscopy and mass determination. *Nature*, 169, 366–367.

Berto, P., Gachet, D., Bon, P., Monneret, S., Rigneault, H. (2012). Wide-field vibrational phase imaging. *Physical Review Letters*, 109, 093902.

Bon, P. (2011). Imagerie microscopique de champs électromagnétiques par interférométrie à décalage quadri-latéral. Applications à la biologie. PhD thesis, Aix-Marseille Université, Marseille.

Bon, P., Maucort, G., Wattellier, B., Monneret, S. (2009). Quadriwave lateral shearing interferometry for quantitative phase microscopy of living cells. *Optics Express*, 17(15), 13080–13094.

Bon, P., Monneret, S., Wattellier, B. (2012a). Non-iterative boundary-artifact free wavefront reconstruction from its derivatives. *Applied Optics*, 51(23), 5698–5704.

Bon, P., Savatier, J., Merlin, M., Wattellier, B., Monneret, S. (2012b). Optical detection and measurement of living cell morphometric features with single-shot quantitative phase microscopy. *Journal of Biomedical Optics*, 17(7), 076004.

Bon, S., Lécart, E., Fort, S., Lévêque-Fort, S. (2014). Fast label-free cytoskeletal network imaging in living mammalian cells. *Biophysical Journal*, 106(8), 1588–1595.

Cuche, E., Bevilacqua, F., Depeursinge, C. (1999). Digital holography for quantitative phase-contrast imaging. *Opt. Lett.*, 24, 291–293.

Doualle, T., Gallais, L., Monneret, S., Bouillet, S., Bourgeade, A., Ameil, C., Lamaignere, L., Cormont, P. (2017). CO2 laser microprocessing for laser damage growth mitigation of fused silica optics. *Optical Engineering*, 56(01), 011022.

Douti, L., Chrayteh, M., Aknoun, S., Doualle, T., Hecquet, C., Monneret, S., Gallais, L. (2015). Quantitative phase imaging applied to laser damage detection and analysis. *Applied Optics*, 28(54), 8375–8382.

Gallais, L. and Monneret, S. (2016). Time-resolved quantitative phase microscopy of laser-material interactions using a wavefront sensor. *Optics Letters*, 41(14), 3245–3248.

Khadir, S., Bon, P., Vignaud, D., Galopin, E., McEvoy, N., McCloskey, D., Monneret, S., Baffou, G. (2017). Optical imaging and characterization of graphene and other 2D materials using quantitative phase microscopy. *ACS Photonics*, 4(12), 3130–3139.

Nomarski, G. and Weil, A.R. (1955). Application à la métallographie des méthodes interférentielles à deux ondes polarisées. *Rev. Met. Paris*, 52(2), 121–134.

Primot, J. and Guérineau, N. (2000). Extended Hartmann test based on the pseudoguiding property of a Hartmann mask completed by a phase chessboard. *Appl. Opt.*, 39, 5715–5720.

Primot, J. and Sogno, L. (1995). Achromatic three-wave (or more) lateral shearing interferometer. *J. Opt. Soc. Am. A*, 12(12), 2679.

Radhakrishnan, R., Gallais, L., Monneret, S. (2019). Wavefront sensing applied to determine temperature dependence of liquids. *Applied Optics*, 58(13), 3646–3651.

Robert, H.M.L., Savatier, J., Vial, S., Verghese, J., Wattellier, B., Rigneault, H., Monneret, S., Polleux, J., Baffou G. (2018). Photothermal control of heat-shock protein expression at the single cell level. *Small*, 14(32), 1801910.

Velghe, S., Primot, J., Guérineau, N., Cohen, M., Wattellier, B. (2005). Wave-front reconstruction from multidirectional phase derivatives generated by multilateral shearing interferometers. *Opt. Lett.*, 30, 245–247.

Volkov, V., Zhu, Y., De Graef, M. (2002). A new symmetrized solution for phase retrieval using the transport of intensity equation. *Micron*, 33, 411–416.

Zernike, F. (1935). Das phasenkontrastverfahren bei der mikroskopischen beobachtung. *Z. Tech. Phys.*, 16, 454–457.